

www.acsnano.org

Scalable Synthesis of High Entropy Alloy Nanoparticles by Microwave Heating

Haiyu Qiao, Mahmoud Tamadoni Saray, Xizheng Wang, Shaomao Xu, Gang Chen, Zhennan Huang, Chaoji Chen, Geng Zhong, Qi Dong, Min Hong, Hua Xie, Reza Shahbazian-Yassar, and Liangbing Hu*



Cite This: ACS Nano 2021, 15, 14928-14937



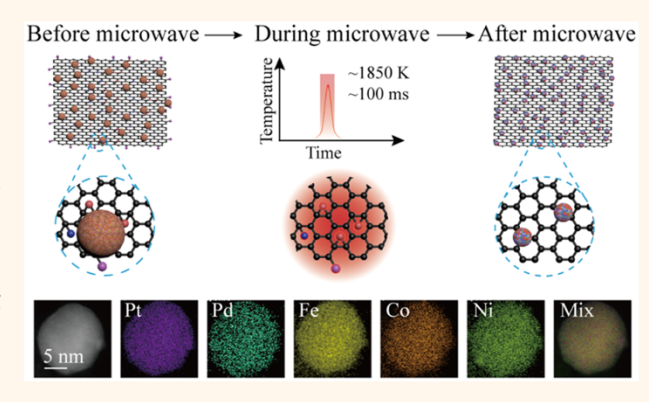
ACCESS

III Metrics & More

Article Recommendations

Supporting Information

ABSTRACT: High entropy alloy nanoparticles (HEA-NPs) are reported to have superior performance in catalysis, energy storage, and conversion due to the broad range of elements that can be incorporated in these materials, enabling tunable activity, excellent thermal and chemical stability, and a synergistic catalytic effect. However, scaling the manufacturing of HEA-NPs with uniform particle size and homogeneous elemental distribution efficiently is still a challenge due to the required critical synthetic conditions where high temperature is typically involved. In this work, we demonstrate an efficient and scalable microwave heating method using carbon-based materials as substrates to fabricate HEA-NPs with uniform particle size. Due to the abundant functional group defects that can absorb microwave efficiently, reduced graphene oxide is employed as a model substrate to



produce an average temperature reaching as high as ~1850 K within seconds. As a proof-of-concept, we utilize this rapid, high-temperature heating process to synthesize PtPdFeCoNi HEA-NPs, which exhibit an average particle size of ~12 nm and uniform elemental mixing resulting from decomposition nearly at the same time and liquid metal solidification without diffusion. Various carbon-based materials can also be employed as substrates, including one-dimensional carbon nanofibers and three-dimensional carbonized wood, which can achieve temperatures of >1400 K. This facile and efficient microwave heating method is also compatible with the roll-to-roll process, providing a feasible route for scalable HEA-NPs manufacturing.

KEYWORDS: microwave, high entropy alloy, high temperature, nanomanufacturing, reduced graphene oxide

INTRODUCTION

High entropy alloys (HEA) are an emerging group of materials containing five or more metallic elements that are uniformly mixed in a crystalline solid-solution phase that is stabilized by high mixing entropy. HEA nanoparticles (HEA-NPs) have recently received significant attention for energy and catalysis applications due to their advantageous physicochemical properties, including a broad selection of elements, high corrosion resistance, high thermal and chemical stability, enhanced mechanical strength, and increased catalytic activity due to the synergistic catalytic reaction of elements. HEA.

Conventional wet chemistry methods of producing HEA-NPs usually lead to elemental phase separation since most metallic elements are immiscible at thermodynamic equilibrium conditions. Achieving the uniform mixing of more than five elements typically requires the use of extremely high temperatures, followed by "freezing" this nonequilibrium state by rapid cooling with a cooling rate of >10³ K/s. However, traditional furnace heating can only reach temperatures of

 \sim 1300 K, which is too low for effective metallic materials' alloying and insufficient heating/cooling rates of just tens to hundreds of K/min. Moreover, it is difficult to ensure the uniformity of the temperature from the surface to the center of the furnace, which could lead to nanoparticles with possible elemental or phase separation.

To overcome these limitations, rapid heating methods that are not based on conventional furnaces are being developed to enable the synthesis of nonequilibrium materials. For example, the carbothermal shock technique is an innovative batch-to-batch, ultrafast, high-temperature process (>2000 K)

Received: June 15, 2021 Accepted: August 2, 2021 Published: August 23, 2021





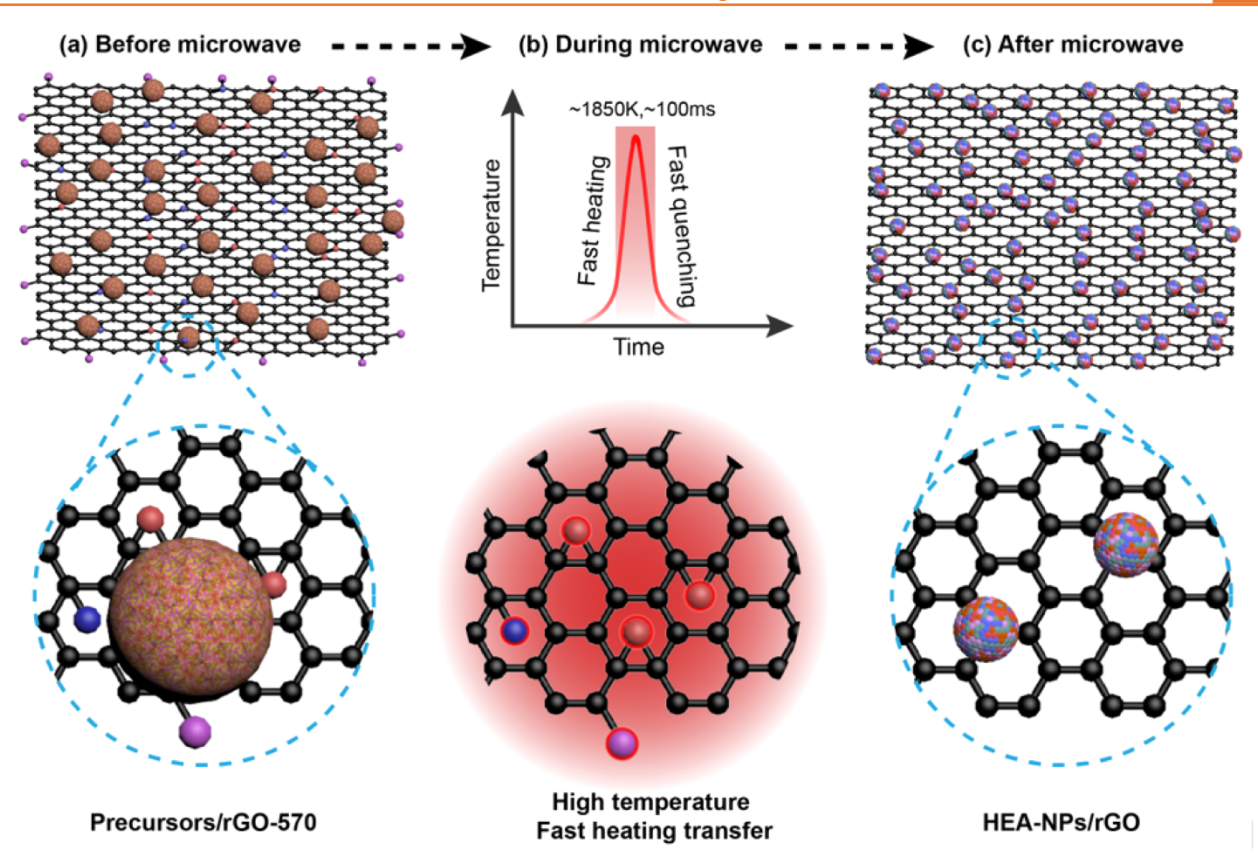


Figure 1. Schematic illustration of the formation of HEA-NPs on rGO by microwave heating. (a) Top: Precursors loaded on the rGO-570 film. Bottom: Magnified view showing the precursor sphere (shown as bigger colorful spheres) composed of mixed metal salts and the rGO-570 film, which has sufficient functional group defects (highlighted as colored spheres). Here, the red, blue, and purple atoms represent epoxy bridges, hydroxyl groups, and carboxyl groups, respectively. (b) Top: Schematic of the heating temperature profile, demonstrating a high temperature of up to ~1850 K within just seconds, as well as a fast heating/quenching process. Bottom: The functional group defects absorb microwave, inducing localized heat that is rapidly transferred through the whole sample. (c) Top: HEA-NPs distributed on the highly reduced rGO film without agglomeration. Bottom: Magnified view showing the monodispersed HEA-NPs.

that can produce uniform, monodisperse HEA-NPs supported on electrically conductive materials. ^{20,24} However, for each batch in the carbothermal shock demonstration, the dimensions of electrically conductive materials are largely limited, leading to challenges in scale-up fabrication. ¹⁹ To tap into the full potential of these materials and their applications, we still need a cost-effective method of continuously fabricating HEA-NPs at large scale.

Microwave heating is an effective way to induce thermal energy and has been used for the synthesis of organic 26 and high-quality carbon materials, $^{27-33}$ as well as carbon-loaded nanomaterials. $^{34-41}$ We demonstrate in this work the use of microwave heating for the rapid and facile synthesis of HEA-NPs, as illustrated in Figure 1. The partially reduced graphene oxide film in argon at ~ 570 K (named rGO-570 film) is employed as a model substrate. For the rGO-570 film, some of functional group defects are eliminated, leading to increased thermal conductivity. 42,43 At the same time, the microwave absorbability is not sacrificed since there are still sufficient functional group defects left.

Before microwave treatment, the rGO-570 film loaded with metal salt precursors (named precursor/rGO-570) is schematically shown in Figure 1a. The small colored spheres connected with the black rGO network represent the remaining functional group defects (including hydroxyl and carboxyl groups, as well as epoxy bridges). The large colorful spheres on top of the rGO describe the metal salt precursor particles. Under

subsequent microwave heating in argon (Figure 1b), the rGO-570 film is able to absorb microwave through the dipoles of the uniformly distributed remaining functional group defects. Due to the high thermal conductivity in rGO-570, the induced localized heat at the defects can then be conducted to the entire sample to achieve uniform heating of the loaded metal salt precursors, which decompose into liquid metals and reduce the rGO-570 to a highly reduced degree. The highly reduced rGO will then tend to reflect rather than absorb microwave because most of the functional group defects are consumed, ceasing the heating process automatically. Subsequently, the rapid quenching of rGO after being reduced at high temperature⁴³ enables direct solidification of the liquid metal into HEA-NPs without elemental or phase separation (Figure 1c). Furthermore, other carbon substrates with different dimensions, such as 1D carbon nanofibers (CNFs) and 3D carbonized wood (c-wood), are also suitable substrates and can induce temperatures of >1400 K while also provide a way of controlling the size of HEA-NPs.

This scalable and facile high-temperature synthesis method induced by microwave heating can be adapted into the roll-to-roll process for the scalable manufacturing of nanomaterials, particularly for use in catalysis and energy.

RESULTS AND DISCUSSION

As a demonstration, we synthesized the PtPdFeCoNi HEANPs on rGO and studied the microwave heating process. We

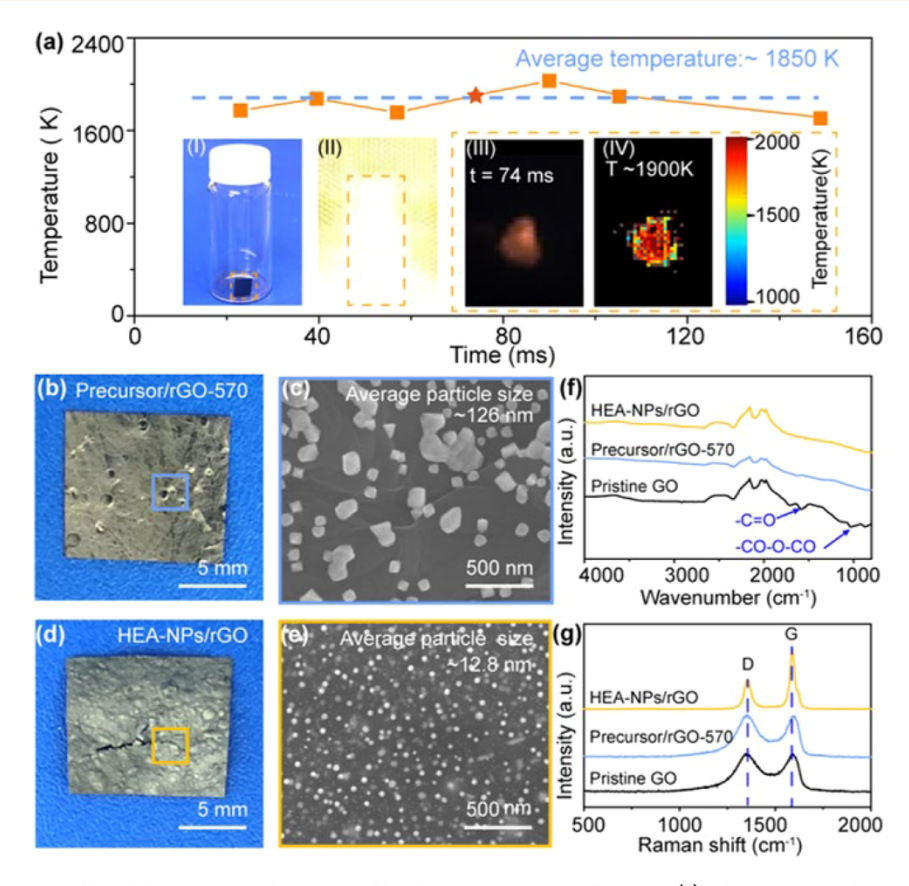


Figure 2. (a) Temperature profile of the precursor/rGO-570 film during microwave heating. (I) The precursor/rGO-570 film highlighted in the orange rectangle is sealed in a vial filled with argon. (II) The precursor/rGO-570 film during the microwave treatment emits glare light. Image captured by the high-speed camera at 74 ms (III) and corresponding temperature color map (IV) confirming a uniform high temperature of ~1900 K on the substrate. Digital image (b) and SEM (c) of the precursor/rGO-570 film. Digital image (d) and SEM (e) of the HEA-NPs/rGO film. The FT-IR (f) and Raman spectra (g) of the pristine GO film, precursor/rGO-570 film, and HEA-NPs/rGO film.

first cast and dried the GO solution into a film at 360 K in the air (named pristine GO film) and then slightly reduced the pristine GO film at ~570 K in argon (named rGO-570 film). Then the precursor with uniformly mixed equal molarities of metal salts (0.01 mol/L of FeCl₃, CoCl₂, NiCl₂, H₂PtCl₆, and PdCl₂, respectively) was drop-cast into the rGO-570 film (named precursor/rGO-570 film) (see more details in Methods).

A piece of the precursor/rGO-570 film in a vial filled with argon is displayed in Figure 2a(I). Then we transferred the vial containing the precursor/rGO-570 film into a microwave oven. After the microwave oven is turned on, the precursor/rGO-570 film emits light (Figure 2a (II); Figure S1). We first characterized the temperature evolution of this microwave heating method by color ratio pyrometry using a high-speed camera according to the gray-body radiation (details shown in the Supporting Information).²² Plasma due to the partially ionized argon in the vial inevitably occurs during microwave (Figure S2),⁴⁴ and it could increase the substrate's temperature according to previous reports. 45-47 However, it is noted that the temperature increase from plasma is not continuous and thus should be secondary for the HEA-NPs formation. In addition, the temperature of plasma cannot be determined by gray-body radiation based on color ratio pyrometry. When calculating the temperature, we cropped the plasma images from the video and only kept the color images belonging to the precursor/rGO-570 film. After ruling out plasma, one consecutive video of joule heating (160 ms) is selected from

the whole process for the pyrometry calculation, and the resulting temperature profile is plotted in Figure 2a. The average temperature of the precursor/rGO-570 film reaches ~1850 K, exceeding the temperature reported by the microwave-induced joule heating of wood (~1400 K)²¹ and rGO powders (~1600 K). 36,48 We attribute the higher temperature observed here to the dense rGO-570 film, which can absorb microwave and convert it to thermal energy more efficiently compared to porous wood or loose rGO powder materials. As an example, at 74 ms (highlighted with a star), the image captured by the high-speed video camera (Figure 2a (III)) and the corresponding temperature color maps (Figure 2a (IV)) demonstrate the temperature is uniformly distributed in the whole rGO-570 film. Selected temperature color maps at multiple stages of heating are shown in Figure S3. This temperature (1850 K) is significantly higher than the decomposition temperature of the precursors and melting points of the metals (Table S1), enabling the decomposition of the precursors and the formation of solid solution particles. The corresponding light intensity (Figure S4) demonstrates a cooling rate of 6×10^4 K/s, which could guarantee the formation of HEA-NPs without elemental and phase separation.

After characterizing the temperature profile during the microwave heating process, we investigated the morphology of the material before and after treatment. Before microwave heating, the surface of the precursor/rGO-570 film (Figure 2b) is flat. A scanning electron microscopy (SEM) image of the

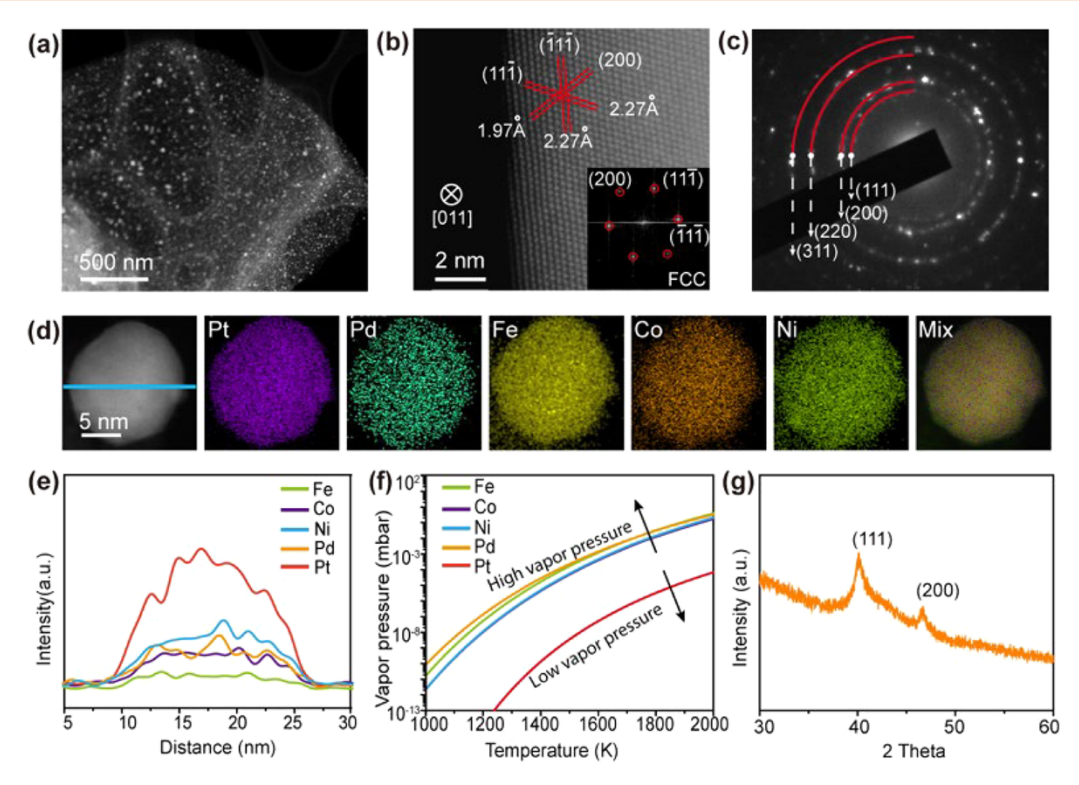


Figure 3. Characterization of the PtPdFeCoNi HEA-NPs on rGO substrates. (a) TEM image, (b) high-resolution TEM image with FFT analysis (inset), and (c) SAED pattern of HEA-NPs on rGO substrates. (d) HAADF-STEM image and STEM-EDS elemental mapping of a PtPdFeCoNi HEA-NPs. (e) EDS line scan along the blue line across the PtPdFeCoNi HEA-NPs shown in (d), demonstrating a solid highentropy particle. (f) Relationship of temperature and vapor pressure for each element in the PtPdFeCoNi HEA-NPs. (g) XRD spectrum of the bulk PtPdFeCoNi HEA-NPs/rGO film, demonstrating an FCC structure.

cross section of the precursor/rGO-570 film (Figure S5a) reveals a relatively dense structure, resulting from the mild reduction of graphene oxide in the argon at 570 K. A further SEM image reveals precursor particles uniformly distributed on the substrate, with an average particle size of ~126 nm and a standard deviation of 58.2 nm (Figure 2c, Figure S6a). The broad X-ray diffraction (XRD) pattern of these separated solid particles on the rGO-570 film also matches well with the standard XRD patterns of the corresponding metal salts as shown in Figure S7, demonstrating these salts' solid particles are microcrystals. We name the sample after microwave heating as the HEA-NPs/rGO film. After microwave heating, obvious bubbles occur on the plicate HEA-NPs/rGO film since gases are rapidly released from the decomposition of precursors and the rapid reduction of rGO-570 film at high temperature (Figure 2d, Figure S5b). After this treatment, nanoparticles are uniformly distributed on the HEA-NPs/rGO film with an average size of ~12 nm and a standard deviation of 5.1 nm (Figure 2e; Figure S6b; 105 particles were measured). These particles exhibit a narrow size distribution, with nearly 95% of the HEA-NPs below 20 nm (Table S2).

The appearance changes from a flat surface to a plicate surface in Figure 2b and d, attributed to the change of functional group defects in the rGO-570 film before and after microwave heating. As shown in Fourier-transform infrared (FT-IR) spectroscopy (Figure 2f), compared to the pristine GO film, the peaks at 1716 cm⁻¹ (corresponding to the functional group of -C=O) and 1154 cm⁻¹ (assigned to the functional group of -CO-C-CO) disappear in the precursor/rGO-570 film, indicating the reduction of the C=O and CO-C-CO functional groups. The difference

between the precursor/rGO-570 film and HEA-NPs/rGO film after microwave heating in FT-IR is slight. Therefore, we employed Raman spectroscopy to better reveal the change in the defects on samples at different stages. The Raman results exhibit an obvious difference between the precursor/rGO-570 film and the HEA-NPs/rGO film after microwave heating (Figure 2g). Compared with the pristine GO film, the intensity ratio of the defect D peak and the graphitic G peak $(I_{D/G})$ of the precursor/rGO-570 film decreases from 1.02 to 1.01, corresponding to the partial reduction of functional group defects in argon at low temperature (570 K). Meanwhile, the $I_{\rm D/G}$ ratio dramatically decreases from 1.01 (the precursor/ rGO-570 film) to 0.52 (the HEA-NPs/rGO film) after microwave heating, demonstrating a strong reduction of the rGO-570 film under the rapid high-temperature microwave process, ⁴⁹⁻⁵¹ in addition to the synthesis of nanoparticles.

Since the defects of rGO are vital for the microwave absorption and thermal conductivity of rGO, we designed a series of control experiments using rGO films with variable defects. The defect degree of rGO films is controlled by varying the reduction time and temperature as shown in Table S3. The defect degree of rGO was measured using Raman spectra and is presented in Figure S8, and we have summarized the results in Table S3 and Figure S9. For the rGO film without further reduction or minor reduction (*i.e.*, a large characteristic defect peak around 1475 cm⁻¹ in the Raman spectra), the rGO film could easily absorb microwave, but could not transfer the heat uniformly due to the high thermal resistance, evidenced by no spot light captured in the microwave oven (Figure S9a,b). For the rGO film with a moderate degree of defects (*i.e.*, rGO-570 film), it could absorb

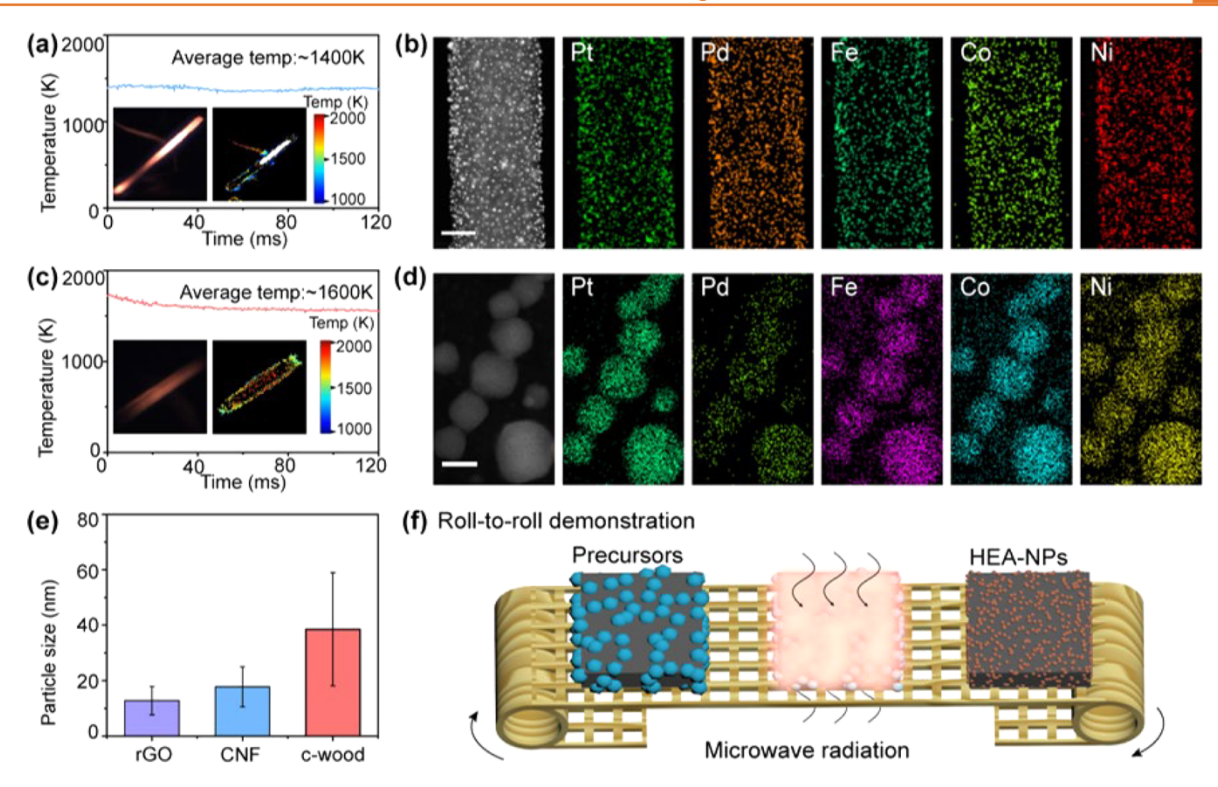


Figure 4. Characterization of PtPdFeCoNi HEA-NPs synthesized on CNFs and c-wood using the microwave heating method. (a) Temperature profile of CNFs during microwave heating. Inset: Image captured by the high-speed camera (left inset) and the corresponding temperature color map (right inset). (b) HAADF-STEM image and STEM-EDS elemental mapping of PtPdFeCoNi HEA-NPs on a single CNF. Scale bar: 100 nm. (c) Temperature profile of c-wood during microwave heating. Inset: Image captured by the high-speed camera (left inset) and the corresponding temperature color map (right inset). (d) HAADF-STEM image and STEM-EDS elemental mapping of PtPdFeCoNi HEA-NPs on c-wood. Scale bar: 10 nm. (e) Particle size comparison of rGO, CNFs, and c-wood. (f) Schematic illustration of the roll-to-roll process for the synthesis of HEA-NPs using the microwave heating method.

microwave efficiently and rapid transfer the heat uniformly on the substrates (Figure S9c). For the rGO film that is overly reduced with a low degree of defects, it would reflect rather than absorb microwave, so there is no uniform light captured (Figure S9d).

In addition, other microwave parameters are also of concern: (1) operating in an air atmosphere would lead to the loss of substrate and the formation of an oxide; that is why HEA-NPs should be synthesized under an atmosphere of inert gas, e.g., Ar.²⁰ (2) Microwave intensity indeed is less important compared to the defects, which is crucial to the absorption of microwave, as previously revealed by our group.⁴⁸ (3) The quenching process plays an extremely important role in the synthesis of HEA-NPs to avoid phase separation due to elemental diffusion.²⁰ Carbon materials have a good thermal conductivity to realize the formation of HEA-NPs.

The reproducibility of materials synthesis relies on a uniform distribution of temperature, which depends on a consistent microwave absorption and a high thermal conductivity of the carbon-based support (parallel experiments of material properties, *i.e.*, composition, size, shape, and substrates size, are provided in Figure S10 and Tables S4 and S5). We found only rGO films with moderate degree of defects could guarantee high temperature at the other parameter set, so we conclude that the reproducibility of materials synthesis could be guaranteed in rGO films with moderate degree of defects.

After we studied the synthesis process, we further characterized the synthesized PtPdFeCoNi HEA-NPs, containing a mixture of noble and transition metals, on rGO. Transmission electron microscopy (TEM) imaging shows the

PtPdFeCoNi HEA-NPs are uniformly monodispersed on the rGO without obvious agglomeration (Figure 3a, Figure S11). The high-angle annular dark field scanning transmission electron microscopy (HAADF-STEM) imaging and fast Fourier transform (FFT) analysis reveal the d-spacing of HEA-NPs to be 2.27, 2.27, and 1.97 Å (Figure 3b, corresponding to (111), (111), and (200) lattice planes, respectively). Combining the distances and angles between lattice planes, we confirm a typical FCC metal structure of HEA-NPs (Figure \$12). The lattice constant of HEA-NPs calculated from FFT results is presented in Table S6. The average lattice constant of the as-prepared PtPdFeCoNi HEA-NPs on rGO is 3.92 Å. We also summarized the lattice constant and d-spacing of the (111) plane and (200) plane for pure Fe, Co, Ni, Pt, and Pd as presented in Table S7. It is clear that the lattice constant of PtPdFeCoNi HEA-NPs is between that of Ni and Pt and is closer to that of Pt. This indicates that HEA-NPs contain more Pt. The material's selected area electron diffraction (SAED) pattern also shows a typical FCC structure with lattice constant 3.872 Å (Figure 3c). The formation of an FCC structure could be attributed to entropydriven mixing and composition effects. 52 With more elements incorporated in the particles, entropy increases, so Gibbs free energy decreases under high temperature. In addition, although Fe has a BCC structure, Co has an HCP structure, most HEA compositions, i.e., Ni, Pt, and Pd, have an FCC structure, and they have a higher tendency to form an FCC structure with less strain in the crystal structure. These results are also consistent with previous reports about the crystal structure of HEA-NPs synthesized with different components

using different methods (the results are summarized in Table S8).

Furthermore, the HAADF-STEM image and energy dispersive X-ray spectroscopy (EDS) elemental mapping of the HEA-NPs demonstrate the homogeneous mixing of Pt, Pd, Co, Fe, and Ni elements within an individual particle, without elemental segregation or phase separation (Figure 3d). The elemental composition is measured by the elemental line scan across the PtPdFeCoNi HEA-NPs marked in blue, and the result in at. % is shown in Figure 3e and Table S9. We found the atomic ratio of Pt was ~3 times higher than that of the other four elements in HEA-NPs, likely due to the different vapor pressures of the metals, which is consistent with the lattice constant results. The relationship of temperature and vapor pressure is described by eq 1:⁵³

$$\log\left(\frac{P}{\text{atm}}\right) = A + B/T + C\log(T) + D/T^3 \tag{1}$$

where P is the vapor pressure, atm is the atmosphere pressure, T is the temperature, and A, B, C, and D are fitting parameters.

The vapor pressure as a function of temperature for different metals is recorded,⁵⁴ and we plotted the results in Figure 3f. In the temperature range shown in the plot (1000-2000 K), the vapor pressure of Pt is significantly lower than that of other metals (i.e., Fe, Co, Ni, and Pd). For instance, the vapor pressure of Pt is $\sim 2.37 \times 10^{-6}$ mbar, which is 4 orders of magnitude lower than that of the other metals (Pd = 0.029mbar, Fe = 0.031 mbar, Co = 0.0115 mbar, and Ni = 0.0137 mbar) at 1800 K (corresponding to our microwave heating temperature). As a result, Pt will evaporate the least compared with the other four elements, which validates the tendency of the atomic ratio when adding the same molar amount of metal salts in the precursors. This temperature—vapor pressure—mass relationship could serve as a theoretical guideline for designing desired elemental ratios. So, if we change the precursor concentration accordingly, e.g., reduce the concentration of Pt to about 1/3, we could achieve an equal molar ratio. Moreover, the XRD results of bulk PtPdFeCoNi HEA-NPs/rGO film (1 × 1 cm) confirm that these five elements are stabilized in a single FCC structure (Figure 3g), consistent with the crystallographic results of a single HEA-NP particle shown in Figure 3b,c.

One more advantage of this microwave heating synthesis method is its superior universality of carbon substrate choices. We conducted the experiments on different dimension carbon material substrates, including 1D CNFs and 3D c-wood. We loaded the same precursors (Pt, Pd, Fe, Co, and Ni metal salts) on CNFs and c-wood by drop-casting (same loading amount with rGO). The CNFs is a typical one-dimensional carbon material with a diameter of ~300 nm (Figure S13). The temperature profile of CNFs during joule heating is represented in Figure 4a, featuring an average temperature of 1400 K for 120 ms before the microwave oven was turned off. A selected snapshot captured by the high-speed camera (left inset) and corresponding temperature color map (right inset) provided in Figure 4a confirm a uniform temperature distribution on CNFs. Selected temperature color maps at other times of CNFs during microwave heating are exhibited in Figure S14, and the relative light intensity (corresponding to temperature) provided in Figure S15 demonstrates the cooling rate of CNFs reaches \sim 7 × 10³ K/s. FT-IR spectra of CNFs showed the defects disappeared after microwave heating (Figure S16a). Correspondingly, the $I_{D/G}$ ratio decreases

from 0.95 to 0.91 (Figure S16b). The TEM imaging demonstrates the HEA-NPs are distributed uniformly on CNFs without aggregation (Figure S17). Low-magnification HAADF image and STEM-EDS elemental maps (Figure 4b) display that these PtPdFeCoNi HEA-NPs are distributed on a single fiber with ultrafine size and high-density dispersion, and these five elements roughly distributed without obvious elemental segregation. Furthermore, STEM-EDS elemental mapping at higher magnification demonstrates the elements are homogeneously distributed within individual particles (Figure S18). The XRD spectrum and STEM imaging with FFT analysis of HEA-NPs/CNFs also demonstrate an FCC structure (Figures S19 and S20).

In addition to CNFs, we also investigated the microwave heating process on c-wood as a manifestation of a 3D carbon material. The c-wood features many microchannels with thin walls (Figure S21, pore size \sim 50 μ m and wall thickness \sim 1 μ m), which could effectively increase the surface-volume ratio, resulting in efficient absorption of the microwave rather than reflection or transmission and increased particle loading. During microwave heating, the temperature profile of the cwood reaches 1600 K and the corresponding cooling rate is ~4 \times 10³ K/s (Figures 4c, S22, and S23). FT-IR spectra of c-wood show the defects obviously disappeared after microwave heating and the $I_{\rm D/G}$ ratio decreases from 0.91 to 0.89 after microwave heating, as revealed by Raman spectra (Figure S24). We also synthesized and confirmed PtPdFeCoNi HEA-NPs on the c-wood substrate by HAADF-STEM imaging and STEM-EDS elemental mapping (Figure 4d). The XRD spectrum and STEM imaging with corresponding FFT analysis of HEA-NPs/c-wood also demonstrate an FCC structure (Figures S25 and S26). The composition of HEA-NPs is Fe, Co, Ni, Pt, and Pd and the loading amount is 5 wt % on cwood according to thermogravimetric analysis (Figure S27).

The particle size comparison of the PtPdFeCoNi HEA-NPs on the CNFs and c-wood substrates is shown in Figure 4e and Figure S28, exhibiting that the nanoparticles synthesized on cwood display a large average particle size (~40 nm) compared to that on CNFs (\sim 20 nm). This may be attributed to the lower cooling rate of the three-dimensional c-wood (4×10^3) K/s for c-wood and 7×10^3 K/s for CNFs, respectively), which provides a longer time for the particles to grow. Moreover, the smaller average particle size on the rGO-570 substrate compared to either the CNFs or c-wood may be attributed to the heating time being controlled by the selfextinguishing mechanism of rGO. The heating of rGO automatically stops when the defects are reduced and consumed by the induced high temperature, while the heating of the CNFs or c-wood has to be manually stopped by turning off the microwave oven. Except from the substrates, the particle size could also be controlled by the concentrations of precursors. Increasing the concentrations of precursors from 0.05 M to 0.1 M, the average particle size could increase from 12.8 nm to 31.4 nm with the same loading amount of 150 μ L (Figure S29).

Lastly, compared with other synthesis methods, the microwave heating method possesses several advantages, such as (1) induced ultrahigh heating temperature, up to \sim 1850 K, (2) uniform temperature distribution on substrates, (3) fast heating/quenching rate (rapid heating within seconds and cooling rates reaching >10³ K/s), (4) universality of carbon substrates with various dimensions, and (5) easy to operate with a household microwave oven. With these

advantages, the microwave heating method could be integrated into the roll-to-roll process (Figure 4f) for the scalable manufacturing of nanomaterials.

CONCLUSION

In this study, we demonstrate a facile, efficient, and scalable microwave heating method for the synthesis of HEA-NPs on carbon-based substrates with different dimensions. Prereduction of rGO is necessary to reach a balance between sufficient functional group defects to efficiently absorb the microwave radiation and simultaneously retain the excellent thermal conductivity to rapidly transfer the induced localized heat. After partially reducing the rGO substrate, we were able to achieve an average high temperature of ~1850 K within seconds, which enables the decomposition of the precursors into liquid metal. As a proof-of-concept demonstration, PtPdFeCoNi HEA-NPs with a uniform size distribution of ~12 nm are successfully synthesized without elemental and phase separation. The variations in the elemental ratio of the particles are explained based on the relationship of the temperature-vapor pressure-mass loss, which could be a guideline for achieving targeted composition ratios. In addition to two-dimensional carbon materials such as GO, this microwave HEA-NPs synthesis approach can also be applied to other carbon substrates, including one-dimensional materials such as CNFs and three-dimensional materials such as c-wood, which also provide a dimensional effect on the particle size of the resulting HEA-NPs. This microwave heating method possesses several advantages, including (1) ultrahigh temperature, (2) uniform heating distribution, (3) fast heating and cooling rate (within seconds), (4) applicability to carbon materials with various dimensions, and (5) cost-effectiveness. Given the above advantages, this microwave radiation-induced joule heating method has high potential to be adopted to the roll-to-roll process for the scalable production of nanomateri-

METHODS

Materials. All precursors were purchased from Sigma-Aldrich, including palladium(II) chloride $(PdCl_2, \geq 99.9\%)$, ruthenium(III) chloride hydrate (99.98%), iron(III) chloride hexahydrate (FeCl₃, $\geq 98\%$), nickel(II) chloride hexahydrate (NiCl₂, $\geq 98\%$), cobalt(II) chloride hexahydrate (CoCl₂, 98%), and chloroplatinic acid hydrate (H₂PtCl₆, $\geq 99.9\%$). Polyacrylonitrile (PAN) was also purchased from Sigma-Aldrich.

Synthesis of GO. GO was synthesized using a modified Hummer's method.

Preparation of CNFs. First, polyacrylonitrile (PAN) was dissolved in dimethylformamide (DMF) with a concentration of 8 wt % and stirred for at least 6 h to obtain a transparent solution. Then polyacrylonitrile fibers were obtained through electrospinning the solution using a homemade electro-spinning setup. The voltage is 15 kV, the feeding rate is 1 mL/h, and the spinning distance is 10 cm. The fibers were collected on a rotating drum with a speed of 80 rpm. Next, the fibers were stabilized at ~533 K for 5 h in air and carbonized at 1073 K for 2 h in argon. Finally, the carbonized nanofibers were collected and stored in ambient conditions at room temperature.

Preparation of c-Wood. A piece of basswood (Walnut Hollow Company) with dimensions of 5 cm \times 4 cm \times 0.5 cm (determined by the furnace dimensions) was calcined at 533 K for 6 h in air and at 973 K for 2 h in argon to obtain c-wood. Then the c-wood was stored in ambient conditions at room temperature. The dimensions of the c-wood used in the experiment are \sim 2.5 cm \times 0.4 cm \times 0.2 cm.

Preparation of HEA-NPs/rGO. We first sealed 3 mL of a 4 mg/ mL graphene oxide (GO) solution in a glass bottle, shaken for 10 min and sonicated for at least 30 min before being uniformly cast into a polytetrafluoroethylene (PTFE) plate with a diameter of 5 cm. Then we transferred the plate into an oven in air at ~360 K for 10 h to completely remove the extra water. This film is named the pristine GO film. Further we slightly reduced the pristine GO film in the oven at 570 K for 2 h in argon to achieve a balance of sufficient functional group defects and thermal conductivity. This film is named the rGO-570 film. For the synthesis of FeCoNiPdPt HEA-NPs, 0.1 mmol for each metal salt, including FeCl₃, CoCl₂, NiCl₂, PdCl₂, and H₂PtCl₆, was dissolved in 10 mL of deionized water by sonication for at least 30 s to prepare the mixed precursor. Then 150 μ L of mixed precursor was drop-cast into the rGO-570 film with a loading amount of ~1 μ mol/mm² (named the precursor/rGO-570 film). The precursor/ rGO-570 film was dried in ambient conditions at room temperature and then sealed in a glass bottle in a glovebox filled with argon to avoid oxidation. The glass bottle was then transferred in the microwave oven (Panasonic, 1200 W) for the microwave heating treatment. The heating time of the microwave oven was set as 10 s for a piece of precursor/rGO-570 film. We tested the rGO-570 film with various dimensions as listed in Table S4, which all showed effective microwave heating. The synthesis of the HEA-NPs on the CNFs and c-wood was similar to precursor loadings of $\sim 1 \, \mu \text{mol/mm}^2$.

Temperature Measurements during Microwave Radiation. The temperature of the rGO, CNFs, and c-wood samples during microwave radiation was measured based on the color ratio pyrometry method using a Vision Research Phantom Miro M110 high-speed camera with video recorded at 2000 frames per second based on our previously reported method. ^{22,37,55}

Material Characterization. SEM was conducted on a Hitachi SU-70 field emission microscope at 10 kV for morphological characterization. TEM imaging was obtained with a JEM 2100 LaB6 instrument. STEM imaging was performed by a spherical aberration corrected JEOL JEM-ARM 200 FC STEM equipped with a 200 keV cold field emission gun. EDS elemental mapping was acquired *via* an Oxford X-max 100TLE with a windowless silicon drift corrector. HAADF-STEM imaging with fast Fourier transform analysis was conducted on the digital micrograph software. The SAED analysis was carried out using a JEOL 3010 TEM operated at 300 keV. XRD was performed (Bruker AXS D8 Advanced, WI, USA) with a scan rate of 3°/min. The Raman testing was performed with a Horiba Jobin Yvon Raman microscope, with a laser source of 532 nm.

ASSOCIATED CONTENT

Supporting Information

The Supporting Information is available free of charge at https://pubs.acs.org/doi/10.1021/acsnano.1c05113.

Digital images of the microwave process and the demonstration of plasma, SEM images of precursor/ rGO-570 film, CNFs, and c-wood, particle size distribution of precursor particles and HEA-NPs, XRD spectra of the precursor/rGO-570 film and PtPdFeCoNi HEA-NPs/CNFs, Raman spectra of rGO with different degrees of defects, CNFs, and c-wood, FFT image calculated from HRTEM of PtPdFeCoNi HEA-NPs/ rGO and PtPdFeCoNi HEA-NPs/c-wood, high-speed video image and light intensity of CNFs and c-wood during microwave heating, FR-IR spectra of CNFs and c-wood, TEM images of PtPdFeCoNi HEA-NPs/CNFs and HEA-NPs/c-wood, HAADF-STEM image and STEM-EDS elemental mapping of PtPdFeCoNi HEA-NPs/CNFs and HEA-NPs/c-wood, TGA analysis of PtPdFeCoNi HEA-NPs/c-wood; table summarizing the physicochemical properties of elemental precursor salts and corresponding metals, table of details and results of control experiments of rGO with different size and

different degree of defects, table of reported lattice constant and *d*-spacings of pure metal and HEA-NPs/rGO, and table summarizing reported synthesized HEA-NPs composition, method, and crystal structure (PDF)

AUTHOR INFORMATION

Corresponding Author

Liangbing Hu — Department of Materials Science and Engineering, University of Maryland, College Park, Maryland 20742, United States; ⊙ orcid.org/0000-0002-9456-9315; Email: binghu@umd.edu

Authors

- Haiyu Qiao Department of Materials Science and Engineering, University of Maryland, College Park, Maryland 20742, United States
- Mahmoud Tamadoni Saray Department of Mechanical and Industrial Engineering, University of Illinois at Chicago (UIC), Chicago, Illinois 60607, United States
- Xizheng Wang Department of Materials Science and Engineering, University of Maryland, College Park, Maryland 20742, United States
- Shaomao Xu Department of Materials Science and Engineering, University of Maryland, College Park, Maryland 20742, United States
- Gang Chen Department of Materials Science and Engineering, University of Maryland, College Park, Maryland 20742, United States
- Zhennan Huang Department of Mechanical and Industrial Engineering, University of Illinois at Chicago (UIC), Chicago, Illinois 60607, United States; orcid.org/0000-0002-8431-0270
- Chaoji Chen Department of Materials Science and Engineering, University of Maryland, College Park, Maryland 20742, United States; oorcid.org/0000-0001-9553-554X
- Geng Zhong Department of Materials Science and Engineering, University of Maryland, College Park, Maryland 20742, United States
- Qi Dong Department of Materials Science and Engineering, University of Maryland, College Park, Maryland 20742, United States
- Min Hong Department of Materials Science and Engineering, University of Maryland, College Park, Maryland 20742, United States
- Hua Xie Department of Materials Science and Engineering, University of Maryland, College Park, Maryland 20742, United States
- Reza Shahbazian-Yassar Department of Mechanical and Industrial Engineering, University of Illinois at Chicago (UIC), Chicago, Illinois 60607, United States; orcid.org/0000-0002-7744-4780

Complete contact information is available at: https://pubs.acs.org/10.1021/acsnano.1c05113

Author Contributions

§H.Q., M.T.S., X.W., and S.X. contributed equally to this work. **Author Contributions**

L.H., H.Q., and S.X. designed the experiments. H.Q., S.X., X.W., and G.Z. conducted microwave experiments. M.S., Z.H., H.X., Q.D., and R.S.Y. performed detailed microscopic characterization. X.W. measured the temperature. H.Q. created the 3D illustrations and performed the FT-IR and Raman

experiments. G.C. performed control experiments and TGA characterizations, C.C. commented on all the figures. M.H. conducted XRD characterizations and analysis. All authors discussed the results and commented on the final manuscript.

Notes

The authors declare no competing financial interest.

ACKNOWLEDGMENTS

This work has no direct funding support. We acknowledge the support of the Maryland Nanocenter and its AIMLab. This work made use of the JEOL JEM-ARM200CF in the Electron Microscopy Service (Research Resources Center, UIC). We acknowledge the support from Dylan Kline and Michael R. Zachariah in the temperature measurements. R.S.-Y. acknowledges the financial support from National Science Foundation (DMR-1809439).

REFERENCES

- (1) George, E. P.; Raabe, D.; Ritchie, R. O. High-Entropy Alloys. *Nature Reviews Materials* **2019**, 4 (8), 515.
- (2) Miracle, D. B. High Entropy Alloys as a Bold Step Forward in Alloy Development. *Nat. Commun.* **2019**, *10* (1), 1805.
- (3) Ding, Q.; Zhang, Y.; Chen, X.; Fu, X.; Chen, D.; Chen, S.; Gu, L.; Wei, F.; Bei, H.; Gao, Y.; Wen, M.; Li, J.; Zhang, Z.; Zhu, T.; Ritchie, R. O.; Yu, Q. Tuning Element Distribution, Structure and Properties by Composition in High-Entropy Alloys. *Nature* **2019**, *574* (7777), 223.
- (4) Gerard, A. Y.; Lutton, K.; Lucente, A.; Frankel, G. S.; Scully, J. R. Progress in Understanding the Origins of Excellent Corrosion Resistance in Metallic Alloys: From Binary Polycrystalline Alloys to Metallic Glasses and High Entropy Alloys. *Corrosion* **2020**, *76* (5), 485.
- (5) Waag, F.; Li, Y.; Ziefuß, A. R.; Bertin, E.; Kamp, M.; Duppel, V.; Marzun, G.; Kienle, L.; Barcikowski, S.; Gökce, B. Kinetically-Controlled Laser-Synthesis of Colloidal High-Entropy Alloy Nanoparticles. *RSC Adv.* **2019**, *9* (32), 18547.
- (6) Wu, H.; Lan, D.; Li, B.; Zhang, L.; Fu, Y.; Zhang, Y.; Xing, H. High-Entropy Alloy@air@Ni-NiO Core-Shell Microspheres for Electromagnetic Absorption Applications. *Composites, Part B* **2019**, 179, 107524.
- (7) Zhao, R.-F.; Ren, B.; Zhang, G.-P.; Liu, Z.-X.; Cai, B.; Zhang, J.-j. CoCrxCuFeMnNi High-Entropy Alloy Powders with Superior Soft Magnetic Properties. J. Magn. Magn. Mater. 2019, 491, 165574.
- (8) Löffler, T.; Meyer, H.; Savan, A.; Wilde, P.; Garzón Manjón, A.; Chen, Y.-T.; Ventosa, E.; Scheu, C.; Ludwig, A.; Schuhmann, W. Discovery of a Multinary Noble Metal-Free Oxygen Reduction Catalyst. *Adv. Energy Mater.* **2018**, *8* (34), 1802269.
- (9) Osgood, H.; Devaguptapu, S. V.; Xu, H.; Cho, J.; Wu, G. Transition Metal (Fe, Co, Ni, and Mn) Oxides for Oxygen Reduction and Evolution Bifunctional Catalysts in Alkaline Media. *Nano Today* **2016**, *11* (5), 601.
- (10) Zhang, G.; Ming, K.; Kang, J.; Huang, Q.; Zhang, Z.; Zheng, X.; Bi, X. High Entropy Alloy as a Highly Active and Stable Electrocatalyst for Hydrogen Evolution Reaction. *Electrochim. Acta* **2018**, 279, 19.
- (11) Dai, W.; Lu, T.; Pan, Y. Novel and Promising Electrocatalyst for Oxygen Evolution Reaction Based on MnFeCoNi High Entropy Alloy. *J. Power Sources* **2019**, 430, 104.
- (12) Liu, K.; Zhang, C.; Sun, Y.; Zhang, G.; Shen, X.; Zou, F.; Zhang, H.; Wu, Z.; Wegener, E. C.; Taubert, C. J.; Miller, J. T.; Peng, Z.; Zhu, Y. High-Performance Transition Metal Phosphide Alloy Catalyst for Oxygen Evolution Reaction. ACS Nano 2018, 12 (1), 158
- (13) Jin, Z.; Lv, J.; Jia, H.; Liu, W.; Li, H.; Chen, Z.; Lin, X.; Xie, G.; Liu, X.; Sun, S.; Qiu, H. J. Nanoporous Al-Ni-Co-Ir-Mo High-Entropy Alloy for Record-High Water Splitting Activity in Acidic Environments. *Small* **2019**, *15* (47), 1904180.

- (14) Ding, K.; Cullen, D. A.; Zhang, L.; Cao, Z.; Roy, A. D.; Ivanov, I. N.; Cao, D. A General Synthesis Approach for Supported Bimetallic Nanoparticles via Surface Inorganometallic Chemistry. *Science* **2018**, 362 (6414), 560.
- (15) Xie, P.; Yao, Y.; Huang, Z.; Liu, Z.; Zhang, J.; Li, T.; Wang, G.; Shahbazian-Yassar, R.; Hu, L.; Wang, C. Highly Efficient Decomposition of Ammonia using High-Entropy Alloy Catalysts. *Nat. Commun.* **2019**, *10* (1), 4011.
- (16) Zhu, X.; Zhang, D.; Chen, C.-J.; Zhang, Q.; Liu, R.-S.; Xia, Z.; Dai, L.; Amal, R.; Lu, X. Harnessing the Interplay of Fe—Ni Atom Pairs Embedded in Nitrogen-Doped Carbon for Bifunctional Oxygen Electrocatalysis. *Nano Energy* **2020**, *71*, 104597.
- (17) Nadeem, M.; Yasin, G.; Bhatti, M. H.; Mehmood, M.; Arif, M.; Dai, L. Pt-M Bimetallic Nanoparticles (M = Ni, Cu, Er) Supported on Metal Organic Framework-Derived N-doped Nanostructured Carbon for Hydrogen Evolution and Oxygen Evolution Reaction. *J. Power Sources* 2018, 402, 34.
- (18) Chen, P.-C.; Liu, X.; Hedrick, J. L.; Xie, Z.; Wang, S.; Lin, Q.-Y.; Hersam, M. C.; Dravid, V. P.; Mirkin, C. A. Polyelemental Nanoparticle Libraries. *Science* **2016**, 352 (6293), 1565.
- (19) Yang, Y.; Song, B.; Ke, X.; Xu, F.; Bozhilov, K. N.; Hu, L.; Shahbazian-Yassar, R.; Zachariah, M. R. Aerosol Synthesis of High Entropy Alloy Nanoparticles. *Langmuir* **2020**, *36* (8), 1985.
- (20) Yao, Y.; Huang, Z.; Xie, P.; Lacey, S. D.; Jacob, R. J.; Xie, H.; Chen, F.; Nie, A.; Pu, T.; Rehwoldt, M.; Yu, D.; Zachariah, M. R.; Wang, C.; Shahbazian-Yassar, R.; Li, J.; Hu, L. Carbothermal Shock Synthesis of High-Entropy-Alloy Nanoparticles. *Science* **2018**, 359 (6383), 1489.
- (21) Zhong, G.; Xu, S.; Chen, C.; Kline, D. J.; Giroux, M.; Pei, Y.; Jiao, M.; Liu, D.; Mi, R.; Xie, H.; Yang, B.; Wang, C.; Zachariah, M. R.; Hu, L. Synthesis of Metal Oxide Nanoparticles by Rapid, High-Temperature 3D Microwave Heating. *Adv. Funct. Mater.* **2019**, 29 (48), 1904282.
- (22) Wang, X.; Huang, Z.; Yao, Y.; Qiao, H.; Zhong, G.; Pei, Y.; Zheng, C.; Kline, D.; Xia, Q.; Lin, Z.; Dai, J.; Zachariah, M. R.; Yang, B.; Shahbazian-Yassar, R.; Hu, L. Continuous 2000 K Droplet-to-Particle Synthesis. *Mater. Today* 2020, 35, 106–114.
- (23) Gao, S.; Hao, S.; Huang, Z.; Yuan, Y.; Han, S.; Lei, L.; Zhang, X.; Shahbazian-Yassar, R.; Lu, J. Synthesis of High-Entropy Alloy Nanoparticles on Supports by the Fast Moving Bed Pyrolysis. *Nat. Commun.* **2020**, *11* (1), 2016.
- (24) Yao, Y.; Liu, Z.; Xie, P.; Huang, Z.; Li, T.; Morris, D.; Finfrock, Z.; Zhou, J.; Jiao, M.; Gao, J.; Mao, Y.; Miao, J.; Zhang, P.; Shahbazian-Yassar, R.; Wang, C.; Wang, G.; Hu, L. Computationally Aided, Entropy-Driven Synthesis of Highly Efficient and Durable Multi-Elemental Alloy Catalysts. *Science Advances* **2020**, 6 (11), eaaz0510.
- (25) Wu, M.; Cui, M.; Wu, L.; Hwang, S.; Yang, C.; Xia, Q.; Zhong, G.; Qiao, H.; Gan, W.; Wang, X.; Kline, D.; Zachariah, M. R.; Su, D.; Li, T.; Hu, L. Hierarchical Polyelemental Nanoparticles as Bifunctional Catalysts for Oxygen Evolution and Reduction Reactions. *Adv. Energy Mater.* **2020**, *10* (25), 2001119.
- (26) Kappe, C. O. Controlled Microwave Heating in Modern Organic Synthesis. *Angew. Chem., Int. Ed.* **2004**, 43 (46), 6250.
- (27) Menéndez, J. A.; Arenillas, A.; Fidalgo, B.; Fernández, Y.; Zubizarreta, L.; Calvo, E. G.; Bermúdez, J. M. Microwave Heating Processes Involving Carbon Materials. *Fuel Process. Technol.* **2010**, *91* (1), 1.
- (28) Schwenke, A. M.; Hoeppener, S.; Schubert, U. S. Synthesis and Modification of Carbon Nanomaterials utilizing Microwave Heating. *Adv. Mater.* **2015**, *27* (28), 4113.
- (29) Ajayan, P. M.; Terrones, M.; de la Guardia, A.; Huc, V.; Grobert, N.; Wei, B. Q.; Lezec, H.; Ramanath, G.; Ebbesen, T. W. Nanotubes in a Flash–Ignition and Reconstruction. *Science* **2002**, 296 (5568), 705.
- (30) Canal-Rodríguez, M.; Arenillas, A.; Menéndez, J. A.; Beneroso, D.; Rey-Raap, N. Carbon Xerogels Graphitized by Microwave Heating as Anode Materials in Lithium-Ion Batteries. *Carbon* **2018**, 137, 384.

- (31) Jiang, W.-S.; Yang, C.; Chen, G.-X.; Yan, X.-Q.; Chen, S.-N.; Su, B.-W.; Liu, Z.-B.; Tian, J.-G. Preparation of High-Quality Graphene Using Triggered Microwave Reduction under an Air Atmosphere. J. Mater. Chem. C 2018, 6 (7), 1829.
- (32) Wang, D.; Dai, R.; Zhang, X.; Liu, L.; Zhuang, H.; Lu, Y.; Wang, Y.; Liao, Y.; Nian, Q. Scalable and Controlled Creation of Nanoholes in Graphene by Microwave-Assisted Chemical Etching for Improved Electrochemical Properties. *Carbon* **2020**, *161*, 880.
- (33) Voiry, D.; Yang, J.; Kupferberg, J.; Fullon, R.; Lee, C.; Jeong, H. Y.; Shin, H. S.; Chhowalla, M. High-Quality Graphene via Microwave Reduction of Solution-Exfoliated Graphene Oxide. *Science* **2016**, *353* (6306), 1413.
- (34) Hassanpour, M.; Safardoust, H.; Ghanbari, D.; Salavati-Niasari, M. Microwave Synthesis of CuO/NiO Magnetic Nanocomposites and its Application in Photo-Degradation of Methyl Orange. *J. Mater. Sci.: Mater. Electron.* **2016**, *27* (3), 2718.
- (35) Fei, H.; Dong, J.; Wan, C.; Zhao, Z.; Xu, X.; Lin, Z.; Wang, Y.; Liu, H.; Zang, K.; Luo, J.; Zhao, S.; Hu, W.; Yan, W.; Shakir, I.; Huang, Y.; Duan, X. Microwave-Assisted Rapid Synthesis of Graphene-Supported Single Atomic Metals. *Adv. Mater.* 2018, 30 (35), e1802146.
- (36) Wan, J.; Yao, X.; Gao, X.; Xiao, X.; Li, T.; Wu, J.; Sun, W.; Hu, Z.; Yu, H.; Huang, L.; Liu, M.; Zhou, J. Microwave Combustion for Modification of Transition Metal Oxides. *Adv. Funct. Mater.* **2016**, *26* (40), 7263.
- (37) Zhong, G.; Xu, S.; Cui, M.; Dong, Q.; Wang, X.; Xia, Q.; Gao, J.; Pei, Y.; Qiao, Y.; Pastel, G.; Sunaoshi, T.; Yang, B.; Hu, L. Rapid, High-Temperature, in Situ Microwave Synthesis of Bulk Nanocatalysts. *Small* **2019**, *15* (47), e1904881.
- (38) Saloga, P. E. J.; Thunemann, A. F. Microwave-Assisted Synthesis of Ultrasmall Zinc Oxide Nanoparticles. *Langmuir* **2019**, 35 (38), 12469.
- (39) Tian, Y.; Sarwar, S.; Zheng, Y.; Wang, S.; Guo, Q.; Luo, J.; Zhang, X. Ultrafast Microwave Manufacturing of MoP/MoO2/carbon Nanotube Arrays for High-Performance Supercapacitors. *J. Solid State Electrochem.* **2020**, 24 (4), 809.
- (40) Tian, Y.; Yang, X.; Nautiyal, A.; Zheng, Y.; Guo, Q.; Luo, J.; Zhang, X. One-Step Microwave Synthesis of MoS2/MoO3@Graphite Nanocomposite as an Excellent Electrode Material for Supercapacitors. Advanced Composites and Hybrid Materials 2019, 2 (1), 151.
- (41) Huang, H.; Zhou, S.; Yu, C.; Huang, H.; Zhao, J.; Dai, L.; Qiu, J. Rapid and Energy-Efficient Microwave Pyrolysis for High-Yield Production of Highly-Active Bifunctional Electrocatalysts for Water Splitting. *Energy Environ. Sci.* **2020**, *13* (2), 545.
- (42) Mu, X.; Wu, X.; Zhang, T.; Go, D. B.; Luo, T. Thermal Transport in Graphene Oxide–From Ballistic Extreme to Amorphous Limit. *Sci. Rep.* **2015**, *4*, 3909.
- (43) Renteria, J. D.; Ramirez, S.; Malekpour, H.; Alonso, B.; Centeno, A.; Zurutuza, A.; Cocemasov, A. I.; Nika, D. L.; Balandin, A. A. Strongly Anisotropic Thermal Conductivity of Free-Standing Reduced Graphene Oxide Films Annealed at High Temperature. *Adv. Funct. Mater.* **2015**, 25 (29), 4664.
- (44) Khattak, H. K.; Bianucci, P.; Slepkov, A. D. Linking Plasma Formation in Grapes to Microwave Resonances of Aqueous Dimers. *Proc. Natl. Acad. Sci. U. S. A.* **2019**, *116* (10), 4000–4005.
- (45) Kim, Y.; Song, W.; Lee, S. Y.; Jeon, C.; Jung, W.; Kim, M.; Park, C.-Y. Low-Temperature Synthesis of Graphene on Nickel Foil by Microwave Plasma Chemical Vapor Deposition. *Appl. Phys. Lett.* **2011**, *98* (26), 263106.
- (46) Boas, C. R. S. V.; Focassio, B.; Marinho, E.; Larrude, D. G.; Salvadori, M. C.; Leão, C. R.; dos Santos, D. J. Characterization of Nitrogen Doped Graphene Bilayers Synthesized by Fast, Low Temperature Microwave Plasma-Enhanced Chemical Vapour Deposition. *Sci. Rep.* **2019**, *9* (1), 13715.
- (47) Salvadori, M. C.; Mammana, V. P.; Martins, O. G.; Degasperi, F. T. Plasma-Assisted Chemical Vapour Deposition in a Tunable Microwave Cavity. *Plasma Sources Sci. Technol.* **1995**, 4 (3), 489–494.

- (48) Xu, S.; Zhong, G.; Chen, C.; Zhou, M.; Kline, D. J.; Jacob, R. J.; Xie, H.; He, S.; Huang, Z.; Dai, J.; Brozena, A. H.; Shahbazian-Yassar, R.; Zachariah, M. R.; Anlage, S. M.; Hu, L. Uniform, Scalable, High-Temperature Microwave Shock for Nanoparticle Synthesis through Defect Engineering. *Matter* 2019, 1 (3), 759.
- (49) Lei, Z.; Liu, X.; Wu, Y.; Wang, H.; Jiang, S.; Wang, S.; Hui, X.; Wu, Y.; Gault, B.; Kontis, P.; Raabe, D.; Gu, L.; Zhang, Q.; Chen, H.; Wang, H.; Liu, J.; An, K.; Zeng, Q.; Nieh, T. G.; Lu, Z. Enhanced Strength and Ductility in a High-Entropy Alloy via Ordered Oxygen Complexes. *Nature* **2018**, *563* (7732), *546*.
- (50) Huang, Y.; Gong, Q.; Zhang, Q.; Shao, Y.; Wang, J.; Jiang, Y.; Zhao, M.; Zhuang, D.; Liang, J. Fabrication and Molecular Dynamics Analyses of Highly Thermal Conductive Reduced Graphene Oxide Films at Ultra-High Temperatures. *Nanoscale* **2017**, *9* (6), 2340.
- (51) Wang, Y.; Chen, Y.; Lacey, S. D.; Xu, L.; Xie, H.; Li, T.; Danner, V. A.; Hu, L. Reduced Graphene Oxide Film with Record-High Conductivity and Mobility. *Mater. Today* **2018**, *21* (2), 186.
- (52) Yao, Y.; Huang, Z.; Hughes, L. A.; Gao, J.; Li, T.; Morris, D.; Zeltmann, S. E.; Savitzky, B. H.; Ophus, C.; Finfrock, Y. Z.; Dong, Q.; Jiao, M.; Mao, Y.; Chi, M.; Zhang, P.; Li, J.; Minor, A. M.; Shahbazian-Yassar, R.; Hu, L. Extreme Mixing in Nanoscale Transition Metal Alloys. *Matter* 2021, 4, 2340.
- (53) Alcock, C. B.; Itkin, V. P.; Horrigan, M. K. Vapour Pressure Equations for the Metallic Elements: 298–2500K. *Can. Metall. Q.* 1984, 23 (3), 309.
- (54) Group, T. W. S. P. Vapor Pressure Calculator, https://www.iap. tuwien.ac.at/www/surface/vapor pressure (accessed April 20, 2020).
- (55) Wang, C.; Ping, W.; Bai, Q.; Cui, H.; Hensleigh, R.; Wang, R.; Brozena, A. H.; Xu, Z.; Dai, J.; Pei, Y.; Zheng, C.; Pastel, G.; Gao, J.; Wang, X.; Wang, H.; Zhao, J.-C.; Yang, B.; Zheng, X.; Luo, J.; Mo, Y.; Dunn, B.; Hu, L. A General Method to Synthesize and Sinter Bulk Ceramics in Seconds. *Science* 2020, 368 (6490), 521.